Journal of Engineering Mechanics and Machinery (2025)
Clausius Scientific Press, Canada

DOI: 10.23977/jemm.2025.100107
ISSN 2371-9133 Vol. 10 Num. 1

Handling and Stability Control of Distributed Drive Electric Vehicle Based on Phase Plane

Xiaoliang Zhang

School of Automobile and Traffic Engineering, Jiangsu University, Zhenjiang, Jiangsu, China

Keywords: Active front-wheel steering, direct yaw moment control, chattering of sliding mode control, phase plane, weight optimization

Abstract: This study investigates the coupling and interference effects between Active Front-Wheel Steering (AFS) and Direct Yaw Moment Control (DYC) in distributed drive electric vehicles. To enhance vehicle handling and stability, a coordinated control strategy for AFS and DYC is developed based on phase plane analysis. Utilizing fuzzy control theory, the phase plane is categorized into three distinct regions: a stable region, a coordinated control region, and an unstable region. To precisely compute the additional yaw moment required for stability enhancement, an adaptive sliding mode controller is designed. Furthermore, a joint sliding mode surface is formulated by considering the deviations between the actual and ideal yaw rate and sideslip angle. The weighting of the sliding mode surface is dynamically adjusted in real time using a stability index in conjunction with a cosine function. To optimally distribute the control effort between AFS and DYC, an improved simulated annealing particle swarm optimization algorithm is employed. The proposed control strategy is validated through simulations conducted on CarSim and Simulink platforms. The results demonstrate that the coordinated control system effectively enhances both vehicle handling and stability.

1. Introduction

With the continuous advancement of the automotive industry, active vehicle safety has garnered increasing research attention. As an emerging category of electric vehicles, distributed drive electric vehicles (DDEV) utilize four independently controllable in-wheel motors for propulsion. This configuration offers several advantages, including a compact structural design, high transmission efficiency, and the seamless integration of various active safety technologies [1-3].

As integral components of a vehicle's active safety system, Active Front-Wheel Steering (AFS), Direct Yaw Moment Control (DYC), and Anti-Slip Regulation (ASR) play crucial roles in ensuring vehicle stability [4]. AFS enhances handling stability by regulating the steering actuator to generate an optimal front-wheel angle. However, its effectiveness is constrained by the lateral force limitations of the tires [5]. DYC adjusts the yaw motion the vehicle by controlling the tire's longitudinal force. Especially in extreme conditions, DYC significantly affects vehicle stability control [6,7]. Many scholars have conducted in-depth research in this area. Among them, Zhang et al. [8] designed an adaptive fuzzy sliding mode controller (FSMC) to obtain the additional yaw moment, and established a method to distribute the additional yaw moment to the four in-wheel

motors to improve the handling stability of the DDEV under extreme conditions. Through the active front independent steering system distributing the steering correction angle unevenly on both sides of the wheels, Farazandeh et al. [9] eliminates the possibility of the tire entering the saturation region. There are often multiple subsystems in the chassis.

Due to the overlap in functions and control objectives, interactions among different vehicle control systems may lead to interference and conflicts, thereby compromising overall performance. Vehicle stability assessment serves as the foundation for designing coordinated control strategies [10]. Li et al. [11] proposed a vehicle stability evaluation method based on the phase plane of front and rear tire slip angles, wherein the weight of the sliding surface is adaptively adjusted according to the state's position within the phase plane and its evolving trend. In [12], a stability assessment scheme utilizing a Self-Organizing Feature Map (SOFM) neural network and the K-means clustering algorithm was introduced to evaluate the real-time stability status of vehicles. Additionally, as a time-domain analysis approach, the $\beta - \dot{\beta}$ phase plane method is frequently employed for vehicle stability assessment [13].

Given that different chassis subsystems are suited to distinct driving scenarios, an effective coordinated control strategy is essential to maximizing their performance. To this end, a novel adaptive Linear Quadratic Regulator (LQR) has been developed to enhance vehicle stability through the integration of Four-Wheel Steering (4WS) and Direct Yaw Moment Control (DYC) [14]. Ahmaddian et al. [15] proposed an integrated Multiple-Input Multiple-Output (MIMO) Model Reference Adaptive Control (MRAC) strategy, designing a coordinated control scheme for AFS and DYC based on a stability index. Similarly, Yim et al. [16] introduced a hierarchical control framework that incorporates an adaptive control strategy to improve vehicle handling and yaw stability through the coordination of AFS and DYC. Despite these advancements, limited research has focused on optimizing the intervention timing and intensity of AFS and DYC. Furthermore, AFS performance is constrained by road adhesion conditions, while DYC, although effective in stability enhancement, reduces vehicle speed, thereby impacting handling performance. The challenge in achieving a well-balanced coordination of AFS and DYC lies in simultaneously maintaining both vehicle handling and stability.

This paper proposes a coordinated control system integrating AFS and DYC based on the $\beta - \dot{\beta}$ phase plane. To account for the limitations imposed by the road adhesion coefficient and other influencing factors, the control regions within the $\beta - \dot{\beta}$ phase plane are defined using fuzzy control theory. The vehicle's stability state is then evaluated by determining the region in which the current state point $(\dot{\beta}_0, \beta_0)$ is located. To compute the required additional yaw moment, an Adaptive Sliding Mode Controller (ASMC) is employed, incorporating an adaptive reaching law to mitigate chattering effects inherent in sliding mode control. To maintain both handling performance and stability, the weighting factors of yaw rate and sideslip angle within the joint sliding mode surface are dynamically adjusted based on the stability index. Furthermore, an improved simulated annealing particle swarm optimization algorithm is utilized to allocate the control weights of AFS and DYC in real-time, thereby optimizing the overall performance of the coordinated control system.

2. Vehicle model description

2.1 Two degrees of freedom vehicle model

To determine the ideal values of vehicle yaw rate and sideslip angle, a 2-DOF vehicle model is established, as illustrated in Figure 1. This model accounts for lateral motion along the Y-axis and

yaw motion about the Z-axis, while neglecting the effects of suspension vibrations on vehicle dynamics.

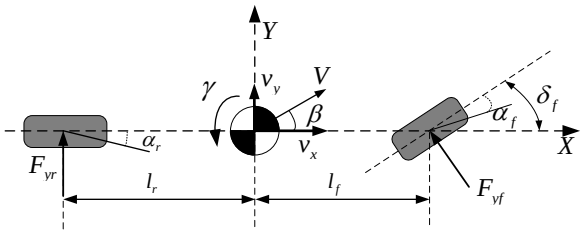

Figure 1: 2-DOF Vehicle model

Vehicle longitudinal dynamic equation:

$$m\left(\dot{v}_y + v_x\gamma\right) = F_{yf}\cos\delta_f + F_{yr} \tag{1}$$

Vehicle yaw dynamic equation:

$$I_z\dot{\gamma} = l_f F_{yf}\cos\delta_f - l_r F_{yr} \tag{2}$$

Where $\dot{v}_y$ is the lateral acceleration, v_x is the longitudinal speed, F_{yf} and F_{yr} are the lateral force of front and rear tires. δ_f is the front wheel angle and I_z is the yaw inertia of the vehicle, l_f and l_r represent the distance from the front and rear axles to the center of mass respectively.

In this model, $\dot{v}_y$ represents the lateral acceleration, while v_x denotes the longitudinal speed. The lateral forces acting on the front and rear tires are represented by F_{yf} and F_{yr}, respectively. δ_f corresponds to the front wheel angle, and I_z signifies the yaw inertia of the vehicle. Additionally, l_f and l_r indicate the distances from the front and rear axles to the vehicle's center of mass, respectively.

The slip angles of the front and rear tires can be approximated using the following expressions: [17]:

$$\begin{cases} \alpha_f = \beta + \dfrac{l_f\gamma}{v_x} - \delta_f \\ \alpha_r = \beta - \dfrac{l_r\gamma}{v_x} \end{cases} \tag{3}$$

The differential equations of formulas (1) and (2) can be expressed as:

$$\begin{cases} \dot{\beta} = -\dfrac{2\left(C_f + C_r\right)}{mV_x}\beta + \left(\dfrac{2\left(l_r C_r - l_r C_f\right)}{mV_x^2} - 1\right)\gamma + \dfrac{2C_f}{mV_x}\delta_f \\ I_z\dot{\gamma} = 2\left(l_r C_r - l_f C_f\right)\beta - \dfrac{2\left(l_f{}^2 C_f + l_r^2 C_r\right)}{V_x}\gamma + 2l_f C_f\delta_f + M_z \end{cases} \tag{4}$$

Where γ is the actual yaw rate of the vehicle, $\dot{\gamma}$ is its derivative, β is the actual sideslip angle of the vehicle, $\dot{\beta}$ is its derivative, C_f and C_r are the tire cornering stiffness.

Convert (4) to state-space equation:

$$\dot{X} = AX + B\delta_f + CU \tag{5}$$

$$X = [\beta \ \gamma]^T \tag{5a}$$

$$A = \begin{bmatrix} a_{11} & a_{12} \\ a_{21} & a_{22} \end{bmatrix} = \begin{bmatrix} -\dfrac{2(C_f + C_r)}{mV_x} & \dfrac{2(l_r C_r - l_r C_f)}{mV_x^2} - 1 \\ \dfrac{2(l_r C_r - l_f C_f)}{I_z} & -\dfrac{2(l_f^2 C_f + l_r^2 C_r)}{I_z V_x} \end{bmatrix} \tag{5b}$$

$$B = [b_1 \ b_2]^T = \begin{bmatrix} \dfrac{2C_f}{mV_x} & \dfrac{2l_f C_f}{I_z} \end{bmatrix}^T \tag{5c}$$

2.2 Tire model

To ensure both accuracy and real-time computational efficiency, a nonlinear tire model is developed based on the Magic Formula. This model employs a combination of trigonometric functions to accurately fit experimental tire test data. The longitudinal force, lateral force, and combined tire forces under various operating conditions are expressed as functions of the slip angle or slip ratio. The Magic Formula model is formulated as follows:

$$F = D\sin(C\arctan(Bx - E(Bx - \arctan Bx))) + s_v \tag{6}$$

Where, F represents lateral force or longitudinal force, x represents slip angle or slip ratio, C is shape factor, B is stiffness factor, E is curvature factor, and s_v is vertical drift.

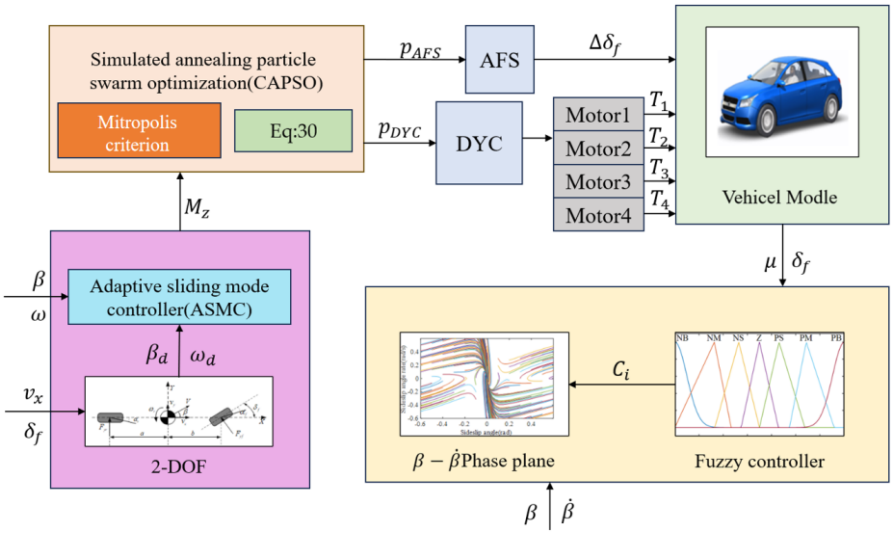

Figure 2:Structure of the coordinated control system

3. Coornianted control system design

The architecture of the proposed coordinated control system is illustrated in Figure 2. This system comprises three key modules: the control region division module, the additional yaw moment decision module, and the weight optimization module.

3.1 Control region division model

As a graphical method， by studying the phase trajectory, we can analyze the vehicle's stable state, equilibrium position, and various parameters' influence on it. The phase planes commonly used to study vehicle stability mainly include $\beta-\dot{\beta}$ and $\beta-\gamma$. Considering the phase trajectory of the $\beta-\gamma$ phase plane is greatly affected by road adhesion coefficient, steering angle, and other parameters, which may result in misjudgment under extreme working conditions. Therefore, the $\beta-\dot{\beta}$ phase plane is selected to judge the current stable state of the vehicle.

Combining the magic tire model with the 2-DOF vehicle model, formula (7) can be expressed as follows:

$$\begin{cases}\dot{\beta}=f_1(\beta,\gamma)\\ \dot{\gamma}=f_2(\beta,\gamma)\end{cases} \tag{7}$$

In this study, the stable region of the phase plane is defined using the two-line method. Within this boundary, any phase trajectory originating from an initial state converges to zero, ensuring stability. The boundary functions of the stable region are expressed as follows:

$$\begin{cases}C_2=C_1\dot{\beta}+\beta\\ C_3=C_1\dot{\beta}+\beta\end{cases} \tag{8}$$

Where C_1 is the boundary slope of the stability region, C_2 and C_3 is the intercept of two boundary functions.

The factors affecting stability region boundary functions parameters include road adhesion coefficient, vehicle speed and steering angle. However, vehicle speed has little influence on the boundary function in practical application, so only the relationship between road adhesion coefficient and steering angle on the boundary function is analyzed. Input vehicle speed $v_x=80km/h$ and steering angle $\delta_f=0$, the phase plane with road adhesion coefficients of 0.8, 0.6, 0.4 , and 0.2 are shown in Figure 3.

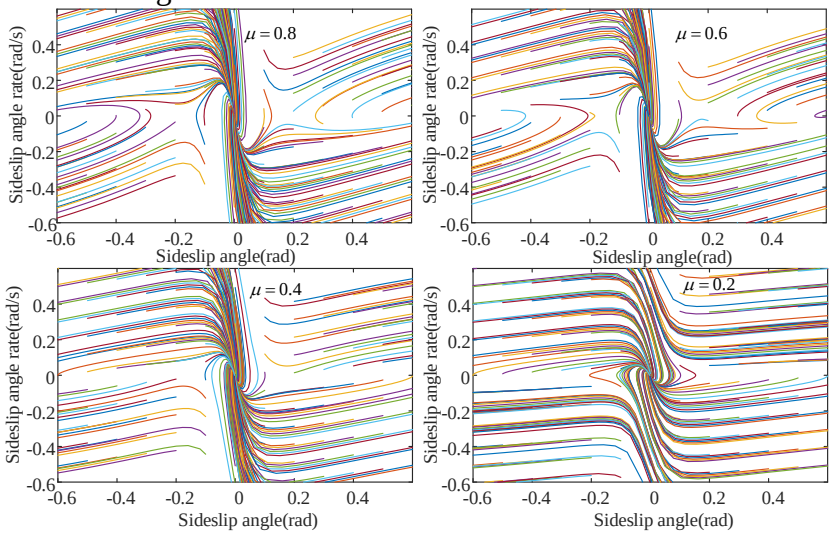

Figure 3: $\beta-\dot{\beta}$ phase plane with different road adhesion coefficients

From Figure.3 can see that the size of the stable area decreases with the road adhesion coefficient.

C_2 and C_3 are symmetrical about the longitudinal axis.

Set the road adhesion coefficient from 0.1 to 0.9 and simulate every 0.1 to obtain the values of C_1, C_2 and C_3, as shown in Table 1.

Table 1: Values of C_1 and C_2 with different road adhesion coefficients

μ	C_1	C_2
0.9	-0.2646	-0.21332
0.8	-0.2985	-0.18403
0.7	-0.3167	-0.15832
0.6	-0.3357	-0.13670
0.5	-0.4348	-0.11823
0.4	-0.4890	-0.09530
0.3	-0.5799	-0.07171
0.2	-0.7628	-0.04010
0.1	-0.9532	-0.02232

Taking μ as the independent variable, the equations of C_2 and C_3 are obtained by polynomial fitting:

$$\begin{aligned} C_1 &= -1.26\mu^2 + 2.064\mu - 1.126 \\ C_2 &= -C_3 = -0.00195\mu^2 - 0.2331\mu + 0.00161 \end{aligned} \tag{9}$$

The same approach is applied to examine the impact of the front wheel angle on the boundary function. Variations in the front wheel angle cause a shift in the vehicle's stability region. The equation of stable area offset o and steering angle is obtained by fitting:

$$o \approx -0.0174\delta_f \tag{10}$$

To control the AFS and DYC, a coordinated control region is divided based on the boundary function of the stable area. This paper selects the internal contraction method to divide the coordinated control region. The boundary of the stability region is extended inward for a certain distance, and the region between the new boundary and the original boundary is taken as the coordinated control region. The division of the control region is shown in Figure 4.

Each area is as follows:

Stable region:

$$C_{2i} < C_1\dot{\beta} + \beta < C_{3i} \tag{11}$$

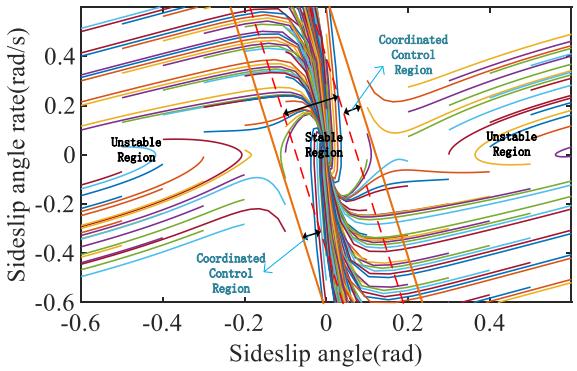

Figure 4: Phase plane control area division

Coordinated control region:

$$\begin{cases} C_2 < C_1\dot{\beta} + \beta < C_{2i} \\ C_{3i} < C_1\dot{\beta} + \beta < C_3 \end{cases} \tag{12}$$

Unstable region:

$$\begin{cases} C_1\dot{\beta} + \beta < C_2 \\ C_1\dot{\beta} + \beta > C_3 \end{cases} \tag{13}$$

Where C_{2i} and C_{3i} are the intercept of the extended boundary function on the horizontal axis, which is obtained by the following formula:

$$\begin{cases} C_{2i} = C_2 \cdot C_i \\ C_{3i} = C_3 \cdot C_i \end{cases} \tag{14}$$

The domain of road adhesion coefficient, steering angle and internal contraction coefficient C_i are $(0.1,1)$, $(-25^\circ, 25^\circ)$ and $(0.3,1)$ respectively. The fuzzy set is $\{NB\ NM\ NS\ Z\ PS\ PM\ PB\}$. Table 2 shows the fuzzy rules.

Table 2: Fuzzy rules

C_i		δ_f						
		NB	NM	NS	z	PS	PM	PB
μ	NB	PB	PB	PB	PM	PB	PB	PB
	NM	PB	PB	PM	PM	PM	PB	PB
	NS	PM	PM	PS	PS	PS	PM	PM
	Z	PM	PM	PS	Z	PS	PM	PM
	PS	PS	PS	Z	NS	Z	PS	PS
	PM	PS	Z	NS	NM	NS	Z	PS
	PB	Z	NS	NM	NB	NM	NS	Z

The membership functions for both input and output variables are illustrated in Figure 5.

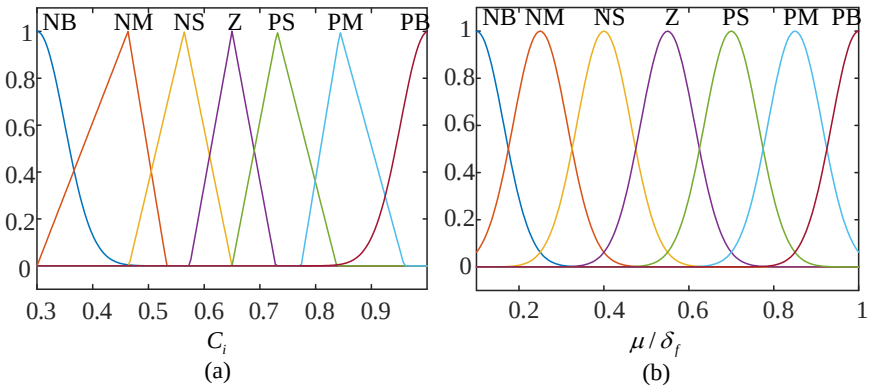

Figure 5: Membership function of input and output

3.2 Additional yaw moment decision module

The additional yaw moment decision module calculates the required yaw moment for vehicle stability. Traditional SMC causes chattering due to its discontinuous control law. To mitigate this, an adaptive sliding mode control (ASMC) method is proposed, balancing response speed and

chattering suppression. In this study, yaw rate and sideslip angle are chosen as control variables, and a joint sliding surface is designed to make the sideslip angle converge to zero and the yaw rate follow its desired value. The joint sliding surface is defined as follows:

$$S = (1-\eta)(\gamma - \gamma_d) + \eta(\beta - \beta_d) \tag{15}$$

Where, η is the weight coefficient.

The expected value γ_d of the yaw rate and the expected value β_d of the sideslip angle are obtained from the formula (4):

$$\gamma_d = \min\left\{\left|\frac{v_x/l}{1+Kv_x^2}\delta_f\right|, |\gamma_{\max}|\right\}\operatorname{sgn}(\delta_f) \tag{16}$$

$$\beta_d = \frac{v_x^2}{l\left(1+Kv_x^2\right)}\left(\frac{l_r}{v_x^2} + \frac{ml_f}{C_r l}\right)\delta_f \tag{17}$$

Where, K represents the stability factor, which is used to characterize the stability of the vehicle. $\gamma_{\max}$ is the maximum yaw rate of the vehicle limited by the road adhesion coefficient. They can be obtained from [19]:

$$K = \frac{m\left(l_f C_f - l_r C_r\right)}{C_f C_r L^2} \tag{18}$$

$$\gamma_{\max} = 0.85\frac{\mu g}{v_x} \tag{19}$$

The differential of equation (15):

$$\dot{S} = \eta\left(\dot{\gamma} - \dot{\gamma}_d\right) + (1-\eta)\left(\dot{\beta} - \dot{\beta}_d\right) \tag{20}$$

An adaptive approach law is introduced to replace the conventional approach law:

$$\dot{S} = -\frac{k}{\lambda}S - \lambda\lfloor S \rfloor \tag{21}$$

Where k is a positive number, $\lfloor S \rfloor$ is a soft symbolic function, and λ is an adaptive coefficient. λ is defined as follows:

$$\dot{\lambda} = \sigma\left(\frac{a|\rho S| + b}{|\rho S| + 1} - \lambda\right) \tag{22}$$

Where a, b and σ are positive numbers,and $a > b$. Adaptive coefficients λ have the following properties:

$$\begin{cases} \lim\limits_{S\to 0}\lambda(\infty) = b \\ \lim\limits_{S\to\infty}\lambda(\infty) = a \end{cases} \tag{23}$$

When S approaches the sliding surface, λ will approach b. The approaching speed of the system is slow, which can effectively suppress the steady-state chattering. At this time, the sign term coefficient λ becomes smaller, which leads to the poor robustness of the system. However the

continuous term coefficient k/λ becomes larger, which improves the system's robustness without enhancing the chattering. When S is far away from the sliding surface, λ will approach a. At this time, the approaching speed of the system is fast, and the system can converge quickly.

The soft symbolic function in the adaptive law is designed to replace the original symbolic function. The soft symbolic function further mitigates system chattering, enhancing control smoothness. The soft symbolic function designed in this paper is as follows:

$$\lfloor S \rfloor = \frac{\varepsilon S}{|\varepsilon S|+1} \tag{24}$$

Where, ε is a positive number.

According to formulas (5), (20), and (21), the output M_z of the sliding mode controller can be obtained as:

$$\begin{aligned} M_z = I_z\left(-\frac{(1-\eta)}{\eta}\left(\dot{\beta}-\dot{\beta}_d\right)+\eta\dot{\gamma}_d\right)-a_{21}\beta-a_{22}\gamma-b_{21}\delta_f \\ +\frac{k}{\lambda}S+\lambda\lfloor S\rfloor \end{aligned} \tag{25}$$

To verify system stability, the Lyapunov function is defined as follows:

$$V = \frac{1}{2}S^2 \tag{26}$$

The derivation of the Lyapunov function is:

$$\dot{V} = S\dot{S} = S\left(-\frac{k}{\lambda}S-\lambda\lfloor S\rfloor\right) \le 0 \tag{27}$$

Formula (26) satisfies $\dot{V} \le 0$, proving that the designed adaptive sliding mode controller is asymptotically stable.

The yaw rate represents the rotational motion of the vehicle around its central axis, while the sideslip angle indicates the deviation from the intended direction. However, when the sideslip angle and its derivative exceed a certain threshold, the yaw rate alone is insufficient to accurately assess vehicle stability. To address this, the region depicted in Figure 6 is defined to regulate the weighting of yaw rate and sideslip angle in the control strategy.

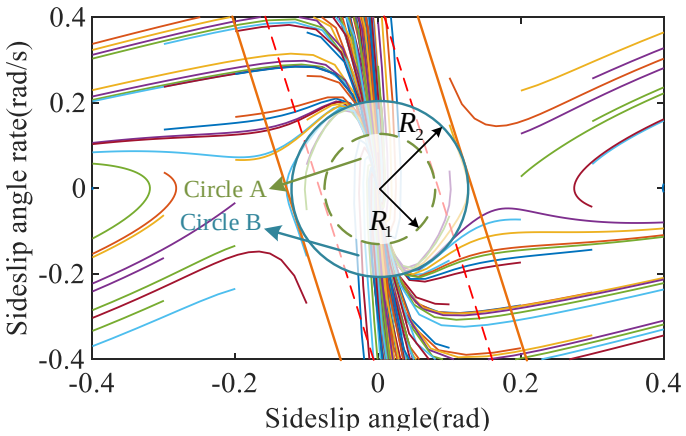

Figure 6: Stability index area division

In Figure 6, circle A and circle B are tangent to the coordination control region's inner and outer

boundary respectively. Define the current vehicle stability state $(\dot{\beta}_0, \beta_0)$ and stability index ξ, where:

$$\xi = \sqrt{\beta_0^2 + \dot{\beta}_0^2} \tag{28}$$

When $\xi < R_1$: The vehicle status point is in circles in circle A, only controlling the yaw rate can maintain vehicle stability.

When $\xi > R_2$: The vehicle status point is out of circle B, and the sideslip angle or its derivative is large. Since the yaw rate alone does not fully represent vehicle stability, the sideslip angle should be used as the primary control target.

When $R_1 < \xi < R_2$: The vehicle status point is located between circle A and circle B. At this stage, the weight of the sideslip angle in the sliding surface should be increased. Let d denote the distance from the current state point to the outer boundary of circle A:

$$d = \frac{\xi - R_1}{R_2 - R_1} \tag{29}$$

To keep the process of weight coefficient variation smooth when $R_1 < \xi < R_2$, take d as the independent variable and use the cosine function to calculate the weight coefficient η.

Based on the above analysis, the weight coefficient η is determined using the following formula:

$$\eta = \begin{cases} 1 & \xi < R_1 \\ \cos(\frac{\pi}{2} d) = \cos(\frac{\pi(\xi - R_1)}{2(R_2 - R_1)}) & R_1 < \xi < R_2 \\ 0 & \xi > R_2 \end{cases} \tag{30}$$

3.3 Weight optimization module

This section presents an improved Simulated Annealing Particle Swarm Optimization (SA-PSO) algorithm for optimizing the weight distribution between AFS and DYC. Considering the distinct characteristics of AFS and DYC, their respective weights are adaptively adjusted based on the control region in which the vehicle state point $(\dot{\beta}_0, \beta_0)$ is located. The corresponding control weights are provided in Table 3.

Table 3: weight coefficient of controller

Control region	AFS weight	DYC weight
Stable region	1	0
Coordinated control region	p_{AFS}	p_{DYC}
Unstable region	0	1

In the stable region, the tire's lateral force margin remains large, allowing the AFS output weight to be set to 1. In contrast, in the unstable region, tire lateral force is prone to saturation. Therefore, DYC is utilized to regulate the tire's longitudinal force, enhancing stability, with the DYC output weight set to 1. In the coordinated control region, the improved SA-PSO algorithm dynamically determines the weights p_{AFS} and p_{DYC} in real time.

To account for variations among population particles during evolution, the algorithm adaptively

assigns weight factors. This allows for rapid exploration of the search space in the early evolution phase to locate promising regions and accelerates convergence to the optimal solution in later stages. Additionally, simulated annealing is integrated with particle swarm optimization (PSO), employing the Metropolis criterion to determine whether to accept new solutions. This approach enhances the algorithm's capability to escape local optima, improving global optimization performance.

The ratio of the fitness $F(k)$ of the generation k population to the fitness $F(k-1)$ of the previous generation population is defined as the dispersion $f(k)$, which reflects the change in the overall fitness value of population evolution. $f(k)$ can be obtained by the following formula:

$$f(k)=\begin{cases}1 & k=1\\ \dfrac{F(k)}{F(k-1)} & k>1\end{cases} \tag{31}$$

Where, k represents the current number of iterations.

The adaptive inertia weight coefficient is obtained by jointly evolving the dispersion $f(k)$ and *Sigmoid* function.

In the early stage of evolution, the dispersion degree of the two adjacent generations is similar, $f(k)$ fluctuates slightly. Moreover, the adaptive inertia weight coefficient decreases gently to ensure the full global optimization of the population in the early stage of evolution. In the later stage of evolution, $f(k)$ is more sensitive to the change of population dispersion, and the amplitude of adaptive inertia weight coefficient is large, so as to realize accurate local search. The inertia weight coefficient is calculated using the following formula:

$$\omega(k)=\omega_{\max}+(\omega_{\min}-\omega_{\max})\frac{1}{1+\exp\left[-10\varsigma(\dfrac{2k}{f(k)\cdot T_{\max}}-1)\right]} \tag{32}$$

Where, $\omega_{\max}$ and $\omega_{\min}$ are the maximum and minimum inertia weights respectively, 0.95 and 0.4 are taken in this paper. ς is the damping factor, generally $[0,1]$, representsing the maximum number of iterations.

The Mitropolis criterion in the simulated annealing algorithm is introduced into the population iteration to accept the worse solution according to the probability generated by the temperature variable and judge whether to replace the old solution with the new solution. The judgment formula of the Mitropolis criterion is as follows:

$$P_i(k)=\begin{cases}1 & F_i(k)\geq F_g\\ \exp(-\dfrac{F_i(k)-F_g}{T_i}) & F_i(k)<F_g\end{cases} \tag{33}$$

Where $F_i(k)$ is the fitness of the $i-th$ particle in the $k-th$ iteration, F_g is the best fitness of the current population, T_i is the current temperature. The initial temperature is set according to the initial particle optimal value, and the temperature decays with a certain coefficient τ after each iteration.

The annealing formula is as follows:

$$T(k)=\begin{cases}F\left(G_{best}\right)/\log(0.2) & k=1\\ T(k-1)\tau & k>1\end{cases} \tag{34}$$

Where T is the initial temperature and the cooling coefficient τ is 0.95. After each iteration, calculate the difference between the fitness of the updated position and the best fitness of the population to judge whether to accept the poor solution.

Define the objective optimization function as:

$$f=\int_0^t a_1\left|\omega_r-\omega_d\right|+a_2\left|\beta-\beta_d\right|+a_3\left|\dot{\beta}\right|dt \tag{35}$$

Where, a_1, a_2 and a_3 are the weight coefficients of the corresponding parts. The objective function minimizes the errors between the expected and actual values of yaw rate and sideslip angle, while also optimizing the sideslip angle velocity.

4. Simulation

The effectiveness of the AFS and DYC coordinated control system proposed in this study is validated through simulations using the CarSim and Simulink platforms. The hub motor model is implemented in Simulink, while the baseline vehicle model from CarSim is adapted into a four-wheel-drive configuration for simulation. The corresponding vehicle model parameters are listed in Table 4.

Table 4: List of the vehicle model parameters

Parameter	Value
Vehicle mass(m/kg)	1230
Moment of inertia(kg.m^2)	1336.4
Distance from centroid to front axle(m)	1.225
Distance from centroid to rear axle(m)	1.364
Wheel rolling radius(m)	0.325
Front-wheel cornering stiffness (N/rad)	-5780
Rear-wheel cornering stiffness(N/rad)	-66854

Select the Double-lane Change with high and low adhesion coefficients for simulation. This paper selects two schemes for the comparison test with the coordinated control system. "Without control" represents that no controller participates in the vehicle stability control, "AFS" represents an AFS controller based on PID control individually, and "Coordinated control" represents the coordinated control system designed in this paper.

4.1 Double-lane change in high road adhesion coefficient

The simulation is conducted with a vehicle speed of v_x=80*km/h*, a road adhesion coefficient of μ =0.85, and a simulation duration of 12 seconds. The results are presented in Figures 7-8.

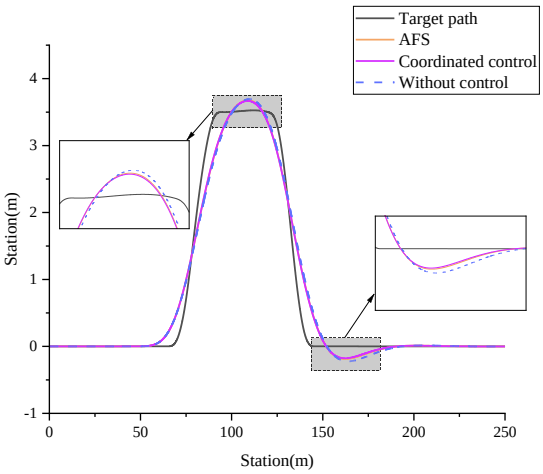

Figure 7: The path tracking accuracy of the Vehicle

Figure 7 illustrates the path tracking accuracy under three different control strategies. Compared to the uncontrolled scenario, both the AFS-only control and the proposed coordinated control strategy exhibit significantly improved path tracking accuracy.

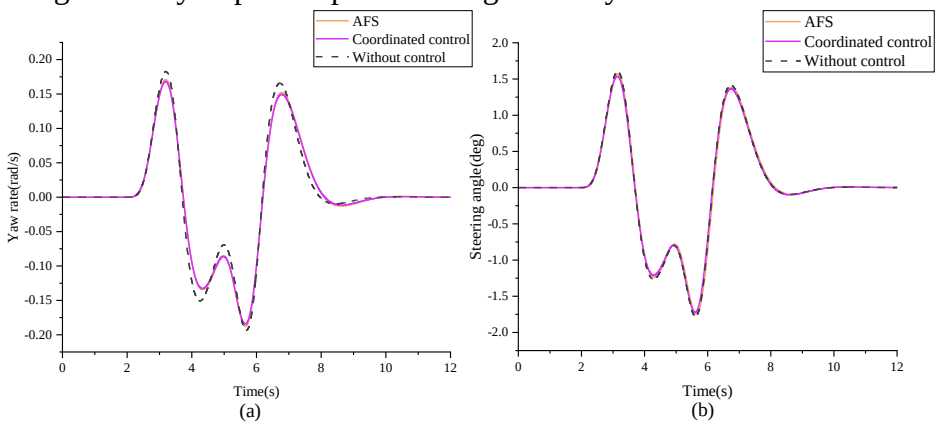

Figure 8: (a) Yaw rate (b) Steering angle

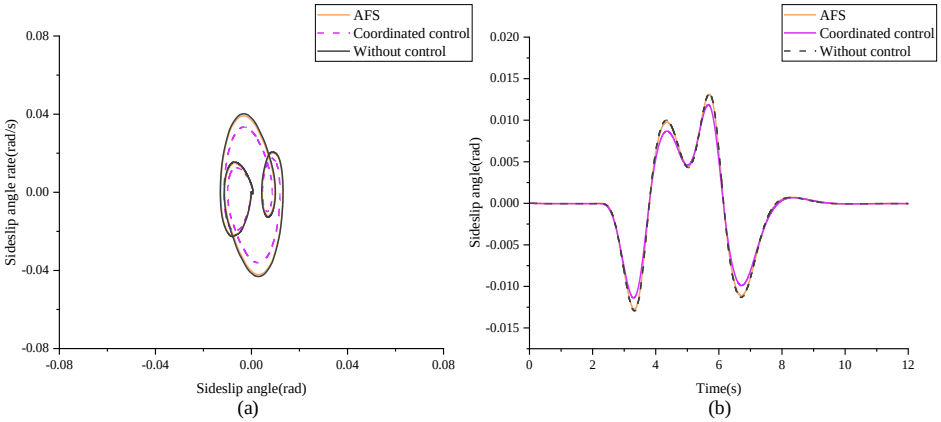

Figure 9: (a) Sideslip angle (b) Phase trajectory portrait

Figures 8(a) and 8(b) depict the yaw rate and steering angle for the three control scenarios. The results show that both AFS-only control and the proposed coordinated control system result in lower yaw rate and front-wheel angle compared to the uncontrolled case. This indicates that both the AFS controller and the coordinated control system enhance vehicle handling performance.

Figures 9(a) and 9(b) are the sideslip angle and the changing trend of $\beta - \dot{\beta}$ phase trajectory of the three cases. It is shown that the peak value of sideslip angle under coordinated control is 0.0117rad，which is 12.74% and 12.39% lower than the AFS control and uncontrolled cases，whose peak value of sideslip angle are 0.01319rad and 0.01315rad respectively. This proves that the coordinated control system and AFS separate control improve the vehicle stability to a certain extent. The changing trend of phase trajectory in Figure 9(b) can also prove this. In addition, the changing trend of AFS control and coordinated control in Figures 7-9 is basically the same. Furthermore the AFS output weight is always 1 in the simulation time, proving that AFS plays a major role in the coordinated control system under high road conditions. The slight variation in the control performance between the AFS-only control and the coordinated control system is attributed to differences in their respective control strategies.

4.2 Double-lane change in low road adhesion coefficient

To evaluate the stability and maneuverability of the coordinated control system under extreme conditions, the simulation is conducted with a vehicle speed of v_x=80*km/h*, a road adhesion coefficient of μ=0.3, and a simulation duration of 12 seconds. The results are presented in Figures 10-13.

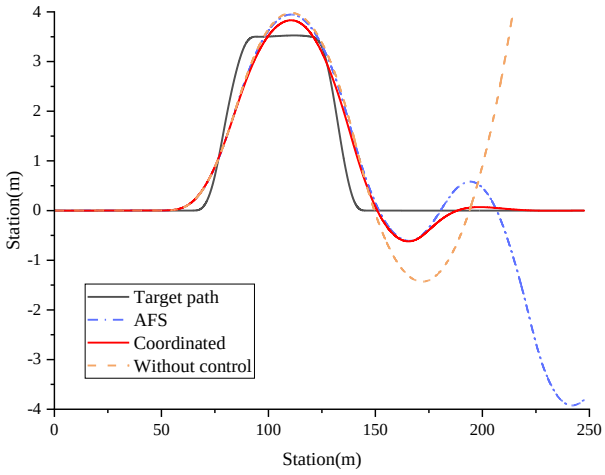

Figure 10: The path tracking accuracy of three cases

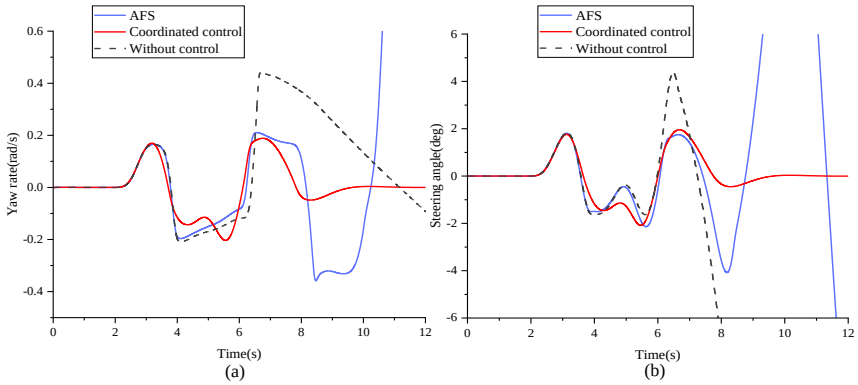

Figure 11: (a) Yaw rate (b) Steering angle

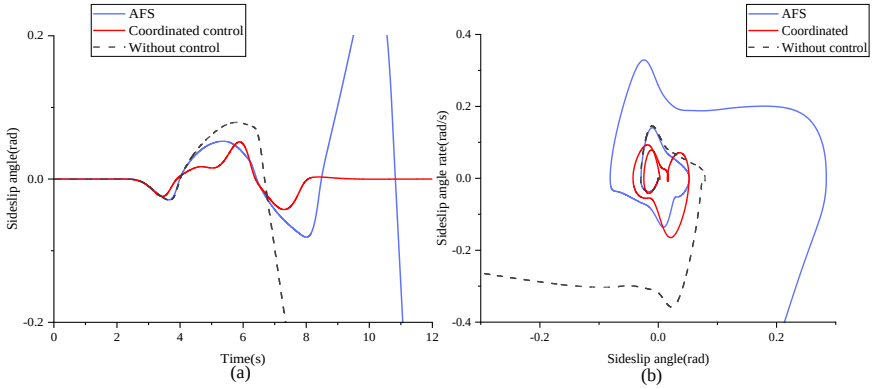

Figure 12: (a) Sideslip angle (b) Phase trajectory portrait

As illustrated in Figure 11, the coordinated control system maintains high path tracking accuracy, with a maximum deviation of 0.621 m. In contrast, vehicles under AFS-only control and no control exhibit significant deviations from the reference path at 170 m and 190 m, respectively. This deviation occurs due to tire lateral force saturation, where excessive front-wheel angles further destabilize the vehicle.

Figures 11(a) and 11(b) depict the yaw rate and steering angle under different control strategies. The coordinated control system effectively regulates these parameters, with maximum values of -0.20364 rad for yaw rate and -2.08644 °for steering angle. In contrast, under AFS-only control, the yaw rate and steering angle undergo sudden changes around the 7th second, indicating a loss of vehicle stability. Figures 12(a) and 12(b) show the sideslip angle and the evolving phase trajectory of β-β. The peak sideslip angle under coordinated control is 0.0519 rad (2.974), with the phase trajectory ultimately converging to the center. However, in the cases of AFS control individually and uncontrolled, the value of sideslip angle suddenly changed in the 8th second and 7th second, and both the phase trajectory did not converge to the center. Figure 13 shows the trend of AFS output weight in the coordinated control system.

From Figure 9 to Figure 13, we can conclude that AFS may fail under extreme working conditions, and the coordinated control system proposed in this paper still has good maneuverability and stability control effect.

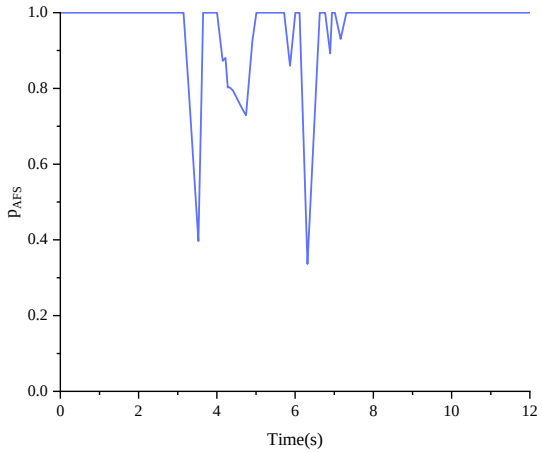

Figure 13: The weight of AFS

5. Conclusion

To enhance vehicle handling and stability while addressing the coupling and conflicts among

chassis subsystems in DDEV, this paper proposes a coordinated control system integrating AFS and DYC. The system consists of three key modules: the control region division module, the yaw moment decision module, and the weight optimization module.

An adaptive control law is designed to mitigate chattering effects in the yaw moment decision module, while the weights of yaw rate and sideslip angle in the sliding mode surface are dynamically adjusted based on the stability index. Additionally, a SA-PSO algorithm is introduced in the weight optimization module to optimize the control weight distribution between AFS and DYC. To validate the effectiveness of the proposed coordinated control system, a co-simulation platform is developed using CarSim and MATLAB/Simulink. Simulations are conducted under double-lane change conditions on both high- and low-adhesion roads. The results demonstrate that the proposed system significantly enhances vehicle handling and stability.

References

[1] Zhong L-H, Nan X, Hong C, et al. (2018) Energy-efficient control of electric vehicles based on linear quadratic regulator and phase plane analysis - ScienceDirect. Applied Energy, 213, 639-657.

[2] Zhu, Z., Chai, X., Xu, L., & Quan, L. (2023). Design and performance of a distributed electric drive system for a series hybrid electric combine harvester. Biosystems Engineering, 236(2), 160-174.

[3] Liu, H., Yan, S., Shen, Y., & Li, C. (2021). Model predictive control system based on direct yaw moment control for 4WID self-steering agriculture vehicle. International Journal of Agricultural and Biological Engineering, 14(2), 175-181.

[4] Xiong L, Yu Z, Han W. (2017) An Integrated Electro-Hydraulic Brake System—Reimagining New Energy Vehicles: Research Innovations at Tongji University. AAAS Publishing.

[5] Nah J, Yim S. (2021) Vehicle Dynamic Control with 4WS, ESC and TVD under Constraint on Front Slip Angles. Energies, 14, 6306.

[6] Xie J, Xu X, Wang F, et al. (2021) Coordinated control based path following of distributed drive autonomous electric vehicles with yaw-moment control. Control Engineering Practice, 106, 104659.

[7] Zhang L, Zhang Z-Q, Wang Z-P, et al. (2021) Chassis Coordinated Control for Full X-by-Wire Vehicles-A Review. Chinese Journal of Mechanical Engineering, 34, 1-25.

[8] Zhang H-Z, Liang J-S, JIANG H-B, et al. (2019) Stability research of distributed drive electric vehicle by adaptive direct yaw moment control. IEEE Access, 7, 106225-106237.

[9] Farazandeh A, Ahmed A, Rakheja S. (2015) An independently controllable active steering system for maximizing the handling performance limits of road vehicles. Proceedings of the Institution of Mechanical Engineers, Part D: Journal of Automobile Engineering, 229, 1291-1309.

[10] Wang Y-L, Zong C-F,G H-Y, et al. (2020) Fault-tolerant path-following control for in-wheel-motor-driven autonomous ground vehicles with differential steering. Asian Journal of Control, 22, 1230-1240.

[11] Li X-Y, Xu N, Guo K-H, et al. (2021) An adaptive SMC controller for EVs with four IWMs handling and stability enhancement based on a stability index. Vehicle System Dynamics, 59, 1509-1532.

[12] Feng T, Wang Y-P, Li Q. (2020) Coordinated control of active front steering and active disturbance rejection sliding mode-based DYC for 4WID-EV. Measurement and Control, 53, 1870-1882.

[13] Wang J-X, Wang R-R, Jing H, et al. (2016) Coordinated active steering and four-wheel independently driving/braking control with control allocation. Asian Journal of Control, 18, 98-111.

[14] Chen X-B, Han Y-Q, Hang P. (2019) Researches on 4WIS-4WID Stability with LQR Coordinated 4WS and DYC. The IAVSD International Symposium on Dynamics of Vehicles on Roads and Tracks, 2019. Springer, 1508-1516.

[15] Ahmadian N, Khosravi A, Sarhadi P. (2020) Integrated model reference adaptive control to coordinate active front steering and direct yaw moment control. ISA transactions, 106, 85-96.

[16] Yim S.(2020) Comparison among active front, front independent, 4-wheel and 4-wheel independent steering systems for vehicle stability control. Electronics, 9, 798.

[17] Peng H-N, Wang W-D, An Q, et al. (2020) Path tracking and direct yaw moment coordinated control based on robust MPC with the finite time horizon for autonomous independent-drive vehicles. IEEE Transactions on Vehicular Technology, 69, 6053-6066.

[18] Zhang J, Wang H, Ma M. (2020) Active front steering-based electronic stability control for steer-by-wire vehicles via terminal sliding mode and extreme learning machine. IEEE Transactions on Vehicular Technology, 69, 14713-14726.